



# Research on a quantitative method for three-dimensional computed tomography of chemiluminescence

GONGXI ZHOU,<sup>1,2</sup> FEI LI,<sup>2,\*</sup> KUANLIANG WANG,<sup>3</sup> XIN LIN,<sup>2</sup> AND XILONG YU<sup>2</sup>

<sup>1</sup>School of Engineering Science, University of Chinese Academy of Sciences, Beijing 100049, China

<sup>2</sup>State Key Laboratory of High Temperature Gas Dynamics, Institute of Mechanics, CAS, Beijing 100190, China

<sup>3</sup>School of Aerospace Engineering, Beijing Institute of Technology, Beijing 100081, China

\*Corresponding author: lifei@imech.ac.cn

Received 19 March 2020; revised 6 May 2020; accepted 15 May 2020; posted 15 May 2020 (Doc. ID 393225); published 10 June 2020

To develop a more advanced 3D computed tomography of the chemiluminescence method, the first quantitative 3D diagnosis was realized. The nonlinearity coefficient, the nonuniformity coefficient of the camera response, and various optical fiber attenuation coefficients were obtained through correction experiments. The conversion relationship between the number of photons released by the target object per unit time and the camera gray value at a specified solid angle was also calibrated. To verify the quantitative reconstruction equation, 3D reconstructions of a methane–air flat flame and a simulated phantom were performed for comparison. The method can overcome artificial distortions caused by uncorrected reconstruction. © 2020 Optical Society of America

<https://doi.org/10.1364/AO.393225>

## 1. INTRODUCTION

In recent years, to provide more detailed measurements of flame structures, high-resolution real-time 3D measurements have been achieved in practice, and thus 3D computed tomography of chemiluminescence (3D-CTC) technology has also been developed strongly. Floyd [1] and Lei [2] studied various projection models and reconstruction algorithms systematically, along with the effects of different shooting conditions and noise conditions on the measurement resolution. At the same time, they enabled a significant reduction in the quantity of equipment required to perform CTC, thus making high-resolution 3D measurements more feasible. In their experiments [3], 10 commercial cameras were combined with the principle of mirrors to obtain a multi-directional projection of the flame of interest. After Floyd [3,4] introduced use of a charge-coupled device (CCD) camera as a detector for CTC diagnosis, Kang *et al.* and Ma *et al.* [5–7] used fiber optic bundles in the 3D-CTC diagnostic system, which reduced the number of cameras required and also allowed greater freedom in arrangement of the cameras. The distance between the front end of the optical fiber and the lens can be adjusted to ensure clarity of imaging, and the optical fiber is then connected to the camera. The acquisition of sub-millimeter flame characteristics and 3D measurements at a kilohertz-scale sampling rate in a supersonic burner [8] confirmed the superiority of the 3D-CTC technology with coupled fibers. Unfortunately, in previous studies, 3D-CTC was only used to construct the three-dimensional

structures of flames and perform the related qualitative analysis, but it did not achieve quantitative measurements of the chemiluminescence.

Chemiluminescence is widely used in combustion diagnosis and is the electromagnetic radiation emitted because of de-excitation of the electronically excited species that are formed via chemical reactions in the combustion reaction zone. This means that chemiluminescence can provide information about the conditions in the reaction zone. Furthermore, a number of studies have shown that, under certain limiting conditions, the quantitative chemiluminescence intensity can be used to characterize the heat release rate and the intensity ratio can also be used to measure the equivalent ratio. In dual-propellant rocket engines, combustion instability is a frequent problem. Under the premise that CH\* chemiluminescence can act as an exothermic marker, the use of CH\* chemiluminescence imaging with high frame rates to characterize the reaction zone has become a hot research topic in recent years [9]. Walsh *et al.* [10] measured the distribution of CH\* under different gravity conditions quantitatively and obtained the spatial distribution via an Abel transformation. Anderson *et al.* [11–13] used a detailed chemical kinetics model to investigate the relationship between the chemiluminescence species and the heat release rate; the strong correlation between the release rate and the chemiluminescence was then verified. As the research into the chemical dynamics intensified, numerical simulation of the chemiluminescence gradually became the experimental comparison object. CH\* and OH\* were also added to the

multi-scale simulations as quasi-steady species, and the combustion instability in complex engine combustions was compared with experimental results [14].

An accurate and stable experimental system is a prerequisite for quantitative chemiluminescence measurement based on 3D-CTC. For the needs of high-precision optical measurement, many scholars have studied the nonlinearity and nonuniformity of the CCD. For example, Dunlap proposed a method that uses dynamic loss edges, darker impurities, and the number of impurities to reveal the digital pixel model of the unknown information of pixels [15,16]. Ninkov used the pixel sensitivity function obtained by experimental measurement to improve the accuracy of optical measurement [17,18]. Qiao used the multi-point and multi-segment linear approximation method to eliminate the nonlinear response of the CCD to a certain extent [19]. Aiming at the measurement process of 3D-CTC, various correction methods have been adopted in this paper.

The purpose of this paper is to achieve accurate quantitative chemiluminescence measurement on the basis of correcting the defects of 3D-CTC. As a noncontact and laser-free diagnostic method, this technology can be combined with computational fluid dynamics to provide sufficient data for research into various types of spacecraft propulsion components.

## 2. THEORETICAL BASIS OF QUANTITATIVE 3D-CTC AND CALIBRATION METHODS

As shown in Fig. 1, the traditional experimental equipment for 3D-CTC consists of a CCD camera and a fiber optic bundle. The multi-angle simultaneous projection imaging data obtained from experimental shooting are input into a reconstruction program to obtain a three-dimensional structure of the target object. However, this seemingly simple process has been confirmed to have some errors in this work. In addition, almost all previous studies have performed qualitative analysis of the imaging, and quantitative reconstruction of the chemiluminescence has not been carried out.

In general, the reconstruction process for 3D-CTC technology can be reduced to the process shown in Eq. (1). Here,  $(x', y', z')$  and  $(x, y)$  are the camera coordinate system and the Earth coordinate system, respectively.  $I_m(x, y)$  is the gray value of the flame projection output by the CCD camera,

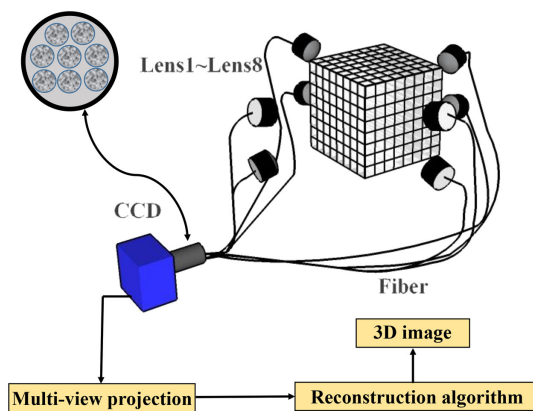


**Fig. 1.** 3D-CTC equipment with fiber bundles and eight lenses, where each lens has a different pitch angle. The squares are the imaging areas.

and  $Q(x', y', z')$  is the 3D information of the flame, which is reproduced using the following reconstruction algorithm:

$$\text{Algorithm } [I_m(x, y)] \rightarrow Q(x', y', z'). \tag{1}$$

Although relative intensity distributions of flames have been realized in previous studies, study of the absolute radiation intensity distribution of the flame has not been completed to date. We know that the camera gray value is closely related to the luminous intensity of the target object. In the forward process of the fiber-based 3D-CTC system, after a photon is released by the target flame and before this photon reaches a pixel, it is affected by the attenuation of both the lens and the optical fiber, the nonuniformity of the pixel, and the response nonlinearity. The final output is a gray value, i.e.,  $I_c(x, y)$ , which is expressed using Eqs. (2)–(4):

$$\eta \times I_m(x, y) = R(x, y) \times \gamma \times k_i \times \theta_i \times N, \tag{2}$$

$$I_c = I_m(x, y) / [R(x, y) \times \gamma \times k_i], \tag{3}$$

$$\text{Algorithm } [\eta \times I_c(x, y)] \rightarrow E(x', y', z'). \tag{4}$$

Here,  $R(x, y)$  is the nonuniformity coefficient of the response between all the camera pixels,  $\gamma$  is the nonlinear coefficient of the pixel under different illuminations, and  $k_i$  represents the different attenuation coefficients of the fiber.  $\theta_i$  represents the solid angles of the different lenses,  $N$  is the total number of photons released by the target object,  $\eta$  is the correspondence coefficient between the unit camera gray value and the number of photons received, and  $E(x', y', z')$  is the accurate number of photons released by the voxel  $(x', y', z')$ . The reconstruction algorithm and the number of lenses were used in most previous studies to improve the reconstruction accuracy [8,20–22]. However, there was barely any consideration of  $R(x, y)$ ,  $\gamma$ , and  $k_i$ , which were treated as constants [23]. The left side of Eq. (2) has the same dimensions as  $E(x', y', z')$ , i.e., *mole-photons*. After all the parameters above have been calibrated,  $I_m(x, y)/[R(x, y) \times \gamma \times k_i]$  can be used rather than  $I_m(x, y)$  to achieve quantitative 3D-CTC.

The fiber-based 3D-CTC system used has been described well in our previous publications [24,25]. Therefore, only a brief description is provided here. A single CCD camera and a custom fiber with eight input bundles and one output were used to achieve eight-angle imaging in a single shot. Each input end in the fiber bundle is a round end with a diameter of 1.5 mm composed of 13,000 fibers, so the total number of fibers used is 104,000. The CCD has  $1024 \times 1040$  pixels with dimensions of  $6.45 \mu\text{m} \times 6.45 \mu\text{m}$ . The calibration equipment (including the solid angles of the different lenses  $\theta_i$ ), methods, reconstruction algorithms, and models of the 3D-CTC system are detailed in [25].

## 3. CALIBRATION

Among the newer types of photoelectric sensors, CCDs [22] have been widely used because of their excellent photoelectric and mechanical characteristics. The nonlinearity and

nonuniformity problems of CCDs and the different attenuation coefficients of the fiber have also been studied extensively [26–30]. During the CCD manufacturing process, it is inevitable that uneven doping concentrations, deposition thickness differences, and lithographic errors will occur. When the finished product is complete, these congenital defects cannot be changed, and this introduces fixed-mode noise that appears as a response rate nonuniformity and dark currents [31,32].

In order to obtain a larger range of illumination adjustment in the experiment, a blackbody furnace and light-emitting diode (LED) backlight board are used. The blackbody furnace adopts a three-stage heating method to heat the body cavity of the blackbody furnace, and uses a high-precision temperature control device to achieve automatic temperature rise and temperature control so that the temperature of the blackbody cavity is very stable, and the floating temperature does not exceed  $0.1^{\circ}\text{C}$ . In addition, when adjusting the illumination of the LED backlight board by adjusting the power of the regulated power supply, the unevenness of the illuminance does not exceed 1%, and it has good time stability.

### A. Nonlinear Coefficient ( $\gamma$ )

With the continuing improvements in the manufacturing levels of blackbodies, the long-term stability of such a body already meets the requirements of a standard device [33]. As shown in Fig. 2(a), the blackbody temperature is fixed at  $700^{\circ}\text{C}$  while the CCD camera front remains perpendicular to the light emission axis.

As an imaging device for high-precision measurements, the output voltage  $V$  (or current  $I$ ) of an ideal detector within the dynamic range should be proportional to the input exposure, i.e.,  $V = c_n * H$  or  $I = c_n * H$ . However, an actual detector generally cannot satisfy the above relationship. The actual relationship is more complex and can be better expressed using polynomial fitting. Let  $H = \Phi t$  be the exposure of a CCD pixel, where  $\Phi$  is the illumination and  $t$  is the integration time

(exposure time). After the CCD response signal is processed using an analog-to-digital converter and a digital signal processor, the gray value (with digital value  $DN$ ) of the pixel is output. The relationship between  $DN$  and the input exposure  $H$  can then be expressed using the following  $n$ th order polynomial [33–36]:

$$DN(H) = \sum_{n=1}^N c_n H^n + DN(0, t), \quad (5)$$

where  $DN(0, t)$  is the dark current of the CCD pixel and  $c_n$  is the response coefficient. Each pixel has the same principle of charge generation, storage, transmission, and detection. Although the response to the same illuminance is different, the response change trend is basically the same as the illuminance changes. Therefore, we use only one response curve to characterize the nonlinearity of the CCD response.

### B. Nonuniformity Coefficient ( $R(x, y)$ )

As shown in Fig. 2(b), a LED backlight board (YL1013, 12 V) was used to provide a uniform light field and a CCD camera (IMI-147FT) was used in combination with a narrow-bandpass filter centered at 430 nm with a 10 nm full width at half-maximum (for the  $\text{CH}^*$  measurements) to record the emission. Before the experiment, the center pixel of the CCD, the imaging axis of the lens, and the center of the LED light emission were aligned accurately to ensure that the angle of the optical axis was  $0^{\circ}$ . Therefore, the adverse effect of the angle of the optical axis on the measurement of the CCD response curve was avoided.

### C. Different Attenuation Coefficients of the Fiber ( $k_i$ )

As mentioned earlier, use of imaging fiber bundles has led to great advances for applications in complex measurement environments such as engines because they can produce multiple image projections simultaneously. This simplifies the difficulty of testing remarkably, and also greatly reduces the experimental equipment costs. Nevertheless, fiber attenuation will inevitably affect the imaging performance. There are numerous sources of attenuation, including absorption attenuation, scattering attenuation, and microbending attenuation. The most important of these sources is the attenuation caused by the absorption of fiber impurities. Impurities in the fiber material, such as hydroxide ions and transition metal ions, have a strong ability to absorb light. Therefore, the experimental equipment described above was also used to investigate the effects of fiber attenuation, as illustrated in Fig. 2(c).

The correspondence coefficient between the unit camera gray value and the number of photons received,  $\eta$ , can be calibrated using a standard tungsten filament lamp (63355, Newport) after adjusting it to the proper orientation and power. The value of  $\eta$  is approximately  $6.3 \times 10^{-17}$  for the CCD settings in our experiments. The calibration method and details of the equipment can be found in our previous study [37].

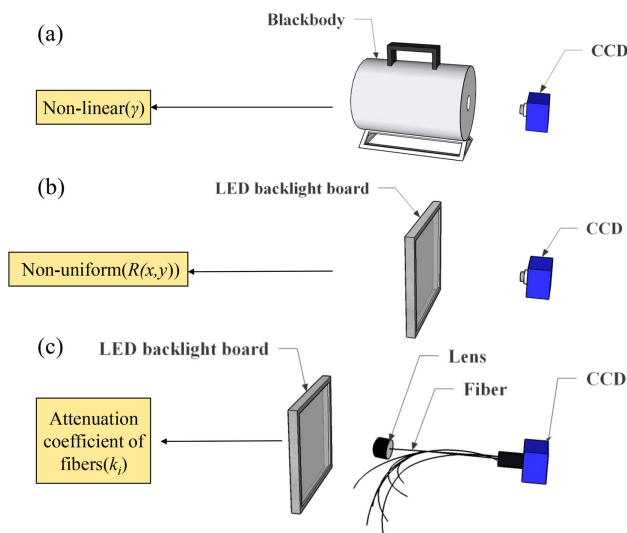


**Fig. 2.** Experimental equipment for calibration: (a) using a blackbody to calibrate the nonlinearity, and (b) and (c) using a light-emitting diode (LED) backlight board to calibrate the nonuniformity and attenuation coefficients of the fibers.

## 4. CALIBRATION RESULTS

Figures 3(a) and 3(b) show the responses of all the pixels of the camera without the lenses and fibers. Overall, the response of

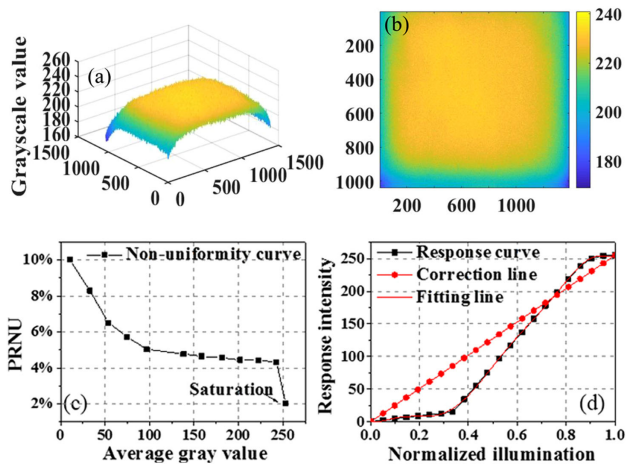


**Fig. 3.** (a) 3D and (b) 2D views of the camera heterogeneity response; (c) the nonuniformity curve between the pixels for the different responses; and (d) the corrected camera response line, the nonlinear response curve, and the fitting line.

the pixels is not uniform. To quantify the heterogeneity characteristics, the nonuniformity of the CCD response is defined as the ratio of the standard deviation of the output signal from each pixel to the average signal, which is the coefficient of variation in statistics and has the symbol PRUN, i.e.,

$$PRUN = \frac{1}{\bar{S}} \sqrt{\frac{1}{xy} \sum_{x=1}^x \sum_{y=1}^y (S(x, y) - \bar{S})^2}, \quad (6)$$

where  $\bar{S}$  is the average gray value of all the pixels, and  $(x, y)$  represents the position of the pixel.

In Fig. 3(c), the PRUN curve shows a downward trend with increasing light intensity, while the unevenness under low light conditions still reaches 6%–10%. The average response to the input light is shown in Fig. 3(d) and can be divided into three parts: the low-response nonlinear region, the approximately linear region, and the saturated nonlinear region. However, an ideal camera should have a linear response, so we want to change this response into a global linear response, as indicated by the red line. Wieldwald and Lerche [38] found a similar falloff response in their image intensifier, where 30% of the output intensity range of the phosphor screen showed obvious nonlinearity. According to the approach introduced in Section 3.A, we used a ninth-order polynomial fit to produce a good fitting curve, which also confirmed the accuracy of Eq. (5). Therefore, in previous 3D-CTC experiments, the defects in these test devices were ignored and the camera was defaulted to have a linear response.

Figure 4 shows the CCD outputs obtained with use of the lens and fibers. Figure 4(a) shows multi-lens imaging. Figure 4(b) shows the sub-images obtained with fiber 4 and lens 4 at different exposure times. The response intensity on these pixels gradually decreases from the center of the circle outward. There is also some speckle noise, indicated by the black circles in Fig. 4(b), which is caused by the different performances of each single fiber in the same bundle. The horizontal and vertical intensity distributions of Fig. 4(b) are then drawn in Fig. 5.

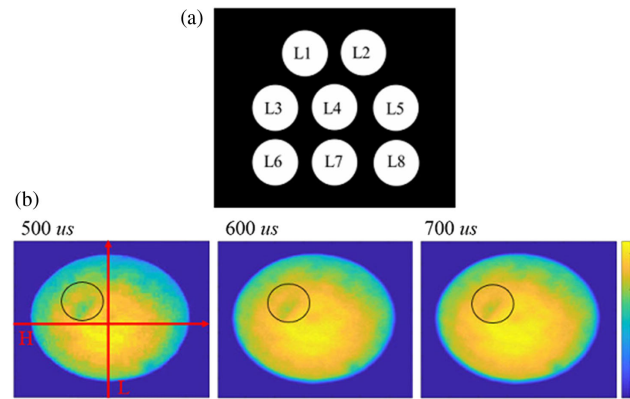


**Fig. 4.** (a) 3D and (b) 2D views of camera heterogeneity response.

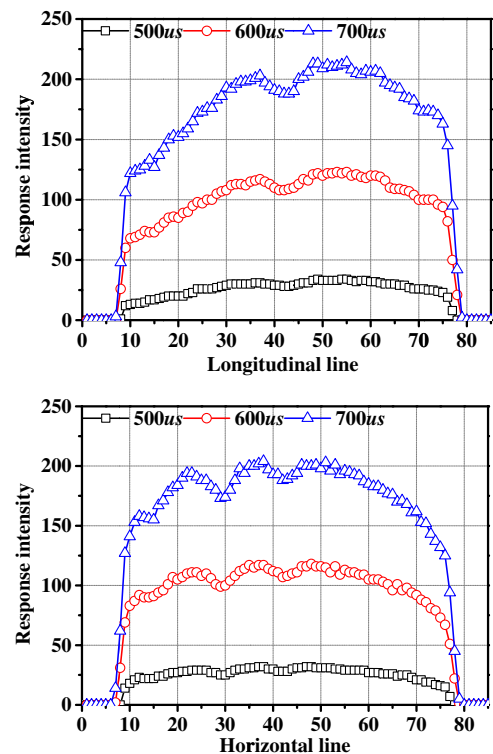


**Fig. 5.** (top) Longitudinal and (bottom) horizontal intensity change curves of the lens at 500  $\mu$ s, 600  $\mu$ s, and 700  $\mu$ s [red straight lines represent  $L$  and  $H$ , as shown in Fig. 4(b)].

Serious nonuniformity is present because of the influence of the manufacturing process and the service life of the fiber bundle, which was mentioned in Section 2. In the 3D-CTC experiments, projections of the target flame should occupy as large a number of pixels as possible for better image reconstruction [39]. As a result, almost all the gray value  $I_m(x, y)$  of the sub-image will be used for reconstruction. Therefore, the nonuniformity caused by the fibers must be taken into account here.

In addition, there is also no consistency of performance between the fiber bundles. To verify this, the responses of all pixels at eight different viewing angles were averaged and the results

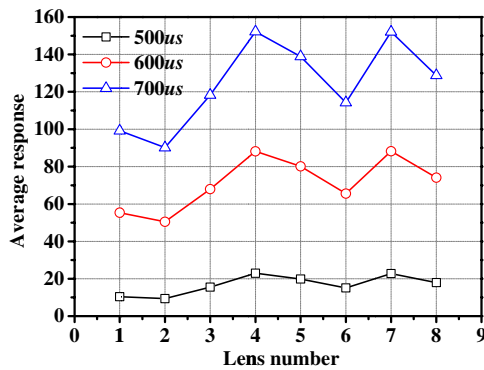


**Fig. 6.** Average responses of different lenses at exposure times of 500  $\mu$ s, 600  $\mu$ s, and 700  $\mu$ s.

are shown in Fig. 6. These results show that the eight fiber bundles did show different performances, while the change trend remains basically the same for the different exposure times. Therefore, the different attenuation coefficients of the fibers,  $k_i$ , are independent of exposure time and can be calibrated using Figs. 4 and 5.

## 5. QUANTITATIVE CHEMILUMINESCENCE MEASUREMENT BASED ON CORRECTED 3D-CTC

Figure 7 shows the entire process of quantitative chemiluminescence measurement based on the correction of 3D-CTC. It can be divided into three steps. The first step is the correction process described in Section 3. The defects of the 3D-CTC implementation process are eliminated by correcting the three coefficients ( $R(x, y)$ ,  $\gamma$ ,  $k_i$ ). The second step is the calibration process. The parameter ( $\eta$ ,  $\theta$ ) was calibrated to achieve the conversion of  $I_m(x, y)$  and  $I_c(x, y)$ . Finally, quantitative chemiluminescence measurement results are obtained through the reconstruction algorithm.

In order to achieve quantitative chemiluminescence intensity measurement, it is necessary to ensure that the original data collected by the 3D-CTC technology is reliable. Currently, various correction methods including the look-up table (LUT) method [40], the radiant response matrix (RRM) method [36], the two-point multi-segment linear approximation method [41], and the photoelectric response nonuniformity correction method [42], have been developed. The LUT and RRM methods are

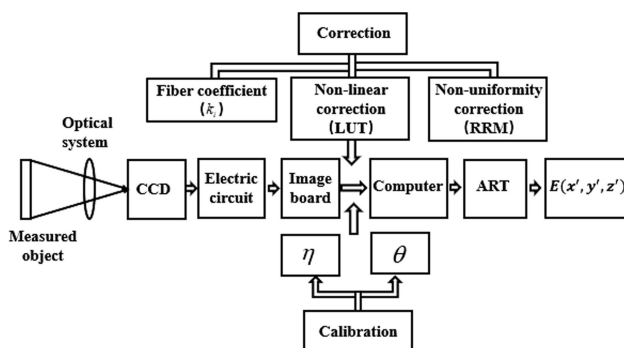


**Fig. 7.** Schematic diagram of quantitative chemiluminescence measurement.

used here because of their simple and high-precision correction effects.

Nonuniformity correction is dependent on establishment of the radiation response matrix using the RRM method. This method treats each pixel as an element in a matrix and then corrects each pixel individually. Finally, all the correction coefficients are formed into an unevenness correction matrix, i.e.,  $R(x, y)$ , in Eq. (2).

The LUT method is used to perform nonlinear correction. Because there are no theoretical data to be used, the actual response curve is measured experimentally and is then corrected to be linear. The specific process is divided into two steps: calibration and compensation. First, the nonlinear response, such as the black square points shown in Fig. 4(d), can be obtained in the calibration process by varying the exposure time. Second, compensation was performed to achieve an ideal straight line response, i.e., the red circles in Fig. 4(d). The output signal value that corresponds to each gray value is then determined from this straight line and a database can thus be established. During the correction process, the LUT method is used to transfer the gray value ( $I_m(x, y)$ ) to the output value. The scale factor between these two values is the nonlinear coefficient, i.e.,  $\gamma$ , in Eq. (2).

## 6. ESTIMATIONS OF EXPERIMENTS AND SIMULATIONS

### A. Experimental Results and Analysis

To evaluate the proposed correction method, an experiment was performed using a flat flame. A  $\text{CH}_4/\text{air}$  premixed burner was used to generate a very stable and flat laminar flame with a diameter of 42 mm. Figure 8(a) shows a photograph of this flame, which is quite uniform. The fiber-based 3D-CTC system described in Section 2 was then used to capture projection images from eight perspectives. The reconstruction target volume is  $7 \times 7 \times 7 \text{ cm}^3$ , and this volume is discretized into  $100 \times 100 \times 100$  matter elements using the algebraic reconstruction technique (ART) algorithm for reconstruction.

Reconstruction results were realized with and without correction and these results are shown in Fig. 8. It is well known that the edge phenomenon caused by ART algorithms is widespread, but it has little effect on the observation of experimental phenomena. Figure 8 shows two obvious features. First, the result with correction is more rounded than the result without correction. Second, the circular flame is highly uniform with correction. Also use Eq. (6) to compare the uniformity before and after correction. In order to avoid the influence of the introduction of the edge area during calculation, the unevenness calculation is affected. The PRUN value is calculated in the flame center area. The unevenness without correction is 6.5% and the unevenness after correction is 1.8%, which shows that the correction effect is obvious. In addition, artifacts have been enhanced with correction. It is because the use of the ART algorithm tends to cause artifacts, and this is difficult to eliminate. In the correction process, according to the correction curve, there is a gain effect on the edge area with a small gray value, which also causes the artifacts to be amplified.

The flame emission intensities along the vertical and horizontal directions were also extracted and are shown in Fig. 9.

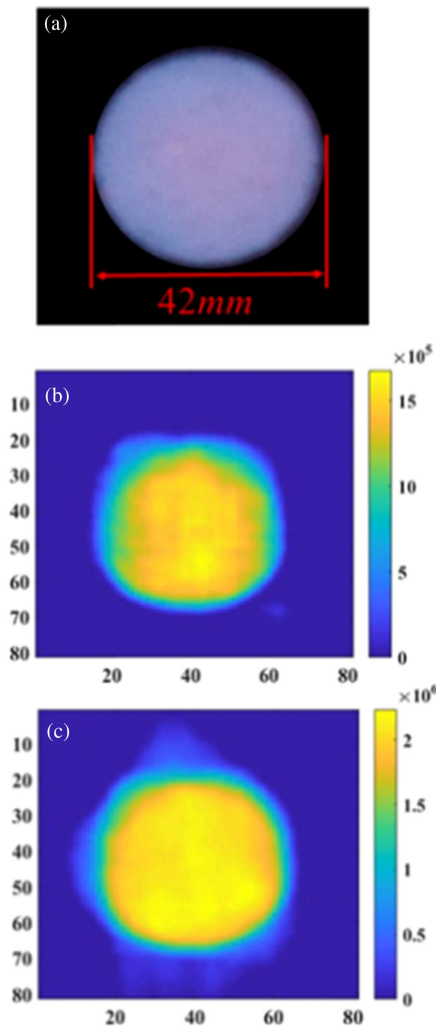


**Fig. 8.** (a) Photograph of a flame taken using a digital camera, where (b) shows the vertical slice reconstruction without correction, and (c) shows the vertical slice with correction.

These images indicate the great advance in the current CTC method. First, to the best of our knowledge, this is the first time that the 3D chemiluminescence distribution has been obtained quantitatively with high spatial resolution. This can be used to provide an important method for engine monitoring [43,44] and can also be used to verify numerical simulations of combustion [45]. Next, the reconstructed result with correction exhibits a much smoother flame luminous intensity, which is closer to the theoretical situation than the result without correction. This indicates that this method can capture the details of the flame structure without distortion.

**B. Simulation and Analysis**

To evaluate the influence of the correction coefficient on the reconstruction, a cube phantom with uniform illumination was used to simulate the correction and reconstruction process. The cube dimensions were 5 cm × 5 cm × 5 cm, while the reconstruction area and the mesh numbers were the same as those used in the experiments. The three correction coefficients  $R(x, y)$ ,  $\gamma$ , and  $k_i$  were coupled as a whole, i.e., using  $f$  as expressed in

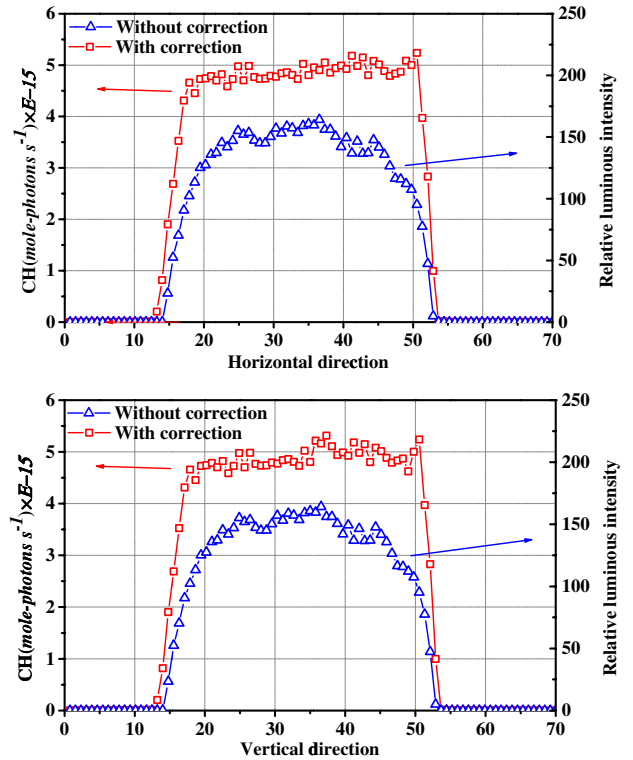


**Fig. 9.** Top: horizontal intensity curve of reconstruction. Bottom: vertical intensity curve of reconstruction.

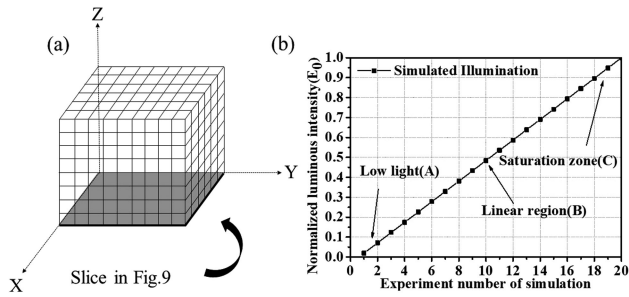
Eq. (7) below. Furthermore,  $E$  is a variable and change in  $E$  causes the projected gray value to pass through three regions. In addition,  $I_m$  and  $I_c$  can be obtained from  $E$  using Eq. (8):

$$f = k_i * R(x, y) * \gamma, \tag{7}$$

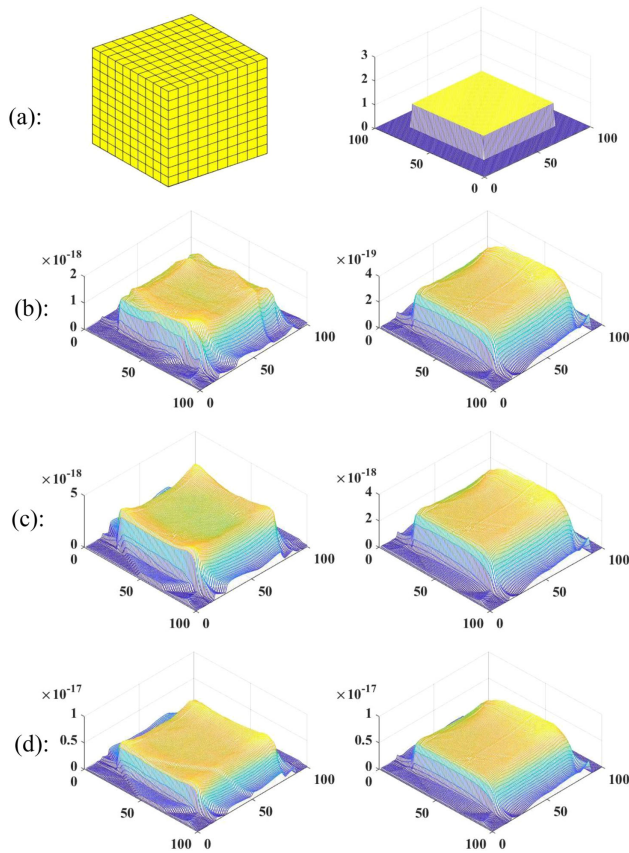
$$\eta \times \frac{I_m}{f} = E. \tag{8}$$

Figure 10(a) shows a schematic diagram of the simulated cube. During the simulation, the normalized emission intensity of the voxel,  $E_0$ , increases linearly and causes the pixel response to pass through the low-response nonlinear region, the approximately linear region, and the saturated nonlinear region, as shown in Fig. 10(b).  $I_m$  can be obtained using projections when setting  $f = 1$ , while  $I_c$  can be obtained via projections using the correction coefficients  $R(x, y)$ ,  $\gamma$ , and  $k_i$ . It should be noted that the calibration coefficients  $\eta$  and  $\theta$  are written into the reconstruction program to compute both  $I_m$  and  $I_c$ . Finally,  $I_c$  and  $I_m$  are used as the input data for the 3D reconstruction.

Figures 11(b)–11(d) show the typical reconstruction results for one slice corresponding to the low-response nonlinear region, the approximately linear region, and the saturated nonlinear region, respectively. The results of the reconstruction with correction are quite smooth and are closer to the input value than the results without correction. In addition, the reconstruction result without correction, named  $E_m$ , is rough and the surface contains large and small protrusions along with pits. Therefore, after the addition of the three types of correction, some of the unevenness phenomena described above are better



**Fig. 10.** (a) Schematic diagram of simulated cube. (b) Average light curve.



**Fig. 11.** (a) Left is a phantom image and right is the uniform luminous intensity distribution of a layer of the phantom. (b)–(d) Intensity (mole-photons/s) distributions of the cube slice. Left: without correction ( $E_m$ ); right: with correction ( $E_c$ ). (b)–(d) correspond to the simulated phantom in the low-response nonlinear region, the approximately linear region, and the saturated nonlinear region, respectively, and the reconstruction results are obtained from the luminous intensity at three points in Fig. 10(b).

resolved. This shows that the correction effect of the proposed procedure is quite considerable.

As a further demonstration of the effect of parameter  $f$  on reconstruction targets with different emission intensities, the error is also defined here. This error is the difference between the reconstructed voxel intensity and  $E$ , which is recorded as  $Er_m$  and  $Er_c$ :

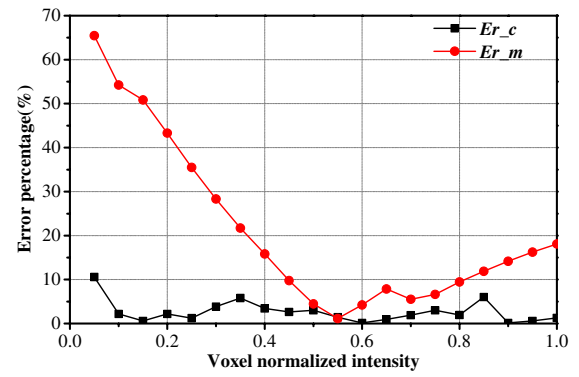


**Fig. 12.** Curves for  $Er_m$  and  $Er_c$ .

$$Er_m = \text{Average} \left( \frac{E_m(x', y', z')}{E(x', y', z')} \right)$$

$$Er_c = \text{Average} \left( \frac{E_c(x', y', z')}{E(x', y', z')} \right). \quad (9)$$

As shown in Fig. 12, the error of the reconstructed intensity without correction initially decreases and then increases along the voxel normalized intensity ( $E_0$ ). The correction in the center linear region has less of an impact on the reconstruction process, and the nonlinear regions at the ends show a significant increase in the error. The maximum error exceeds 50% for small  $E_0$ , which means that the previous 3D-CTC method distorted flame structures with low luminous intensities. In contrast, the reconstruction error with correction has changed slightly for all values of  $E_0$ .

The reconstruction error has dropped significantly with correction, but small deviations still exist. Therefore, in the study of quantitative chemiluminescence intensity, the fiber bundle with less difference between each fiber and the more linear CCD should be selected as much as possible. In addition to this, the calibration process described in this paper is very important. Especially when the luminous intensity of the target object is weak or too strong, otherwise the experimental results will deviate far from the true value.

So far, we have verified the effectiveness of the correction method and quantitative chemiluminescence analysis method adopted in this paper in a uniform flow field through experiments and simulations. In previous studies, the application of 3D-CTC in complex flow fields has been realized. It is worth noting that the calibration and correction methods adopted in this paper are directed to the imaging system and are not limited to the flame itself. Therefore, the quantitative chemiluminescence method described in the paper is expected to be applied to complex flow fields.

## 7. CONCLUSIONS

Quantitative 3D-CTC was achieved for the first time via careful calibration of the imaging-related coefficients. Correction coefficients, including the nonuniformity coefficient of the imaging system,  $R(x, y)$ , the nonlinear coefficient of the pixel under

different illumination conditions,  $\gamma$ , and the different attenuation coefficients of the fibers,  $k_i$ , were measured accurately using a blackbody and an LED backlight board. The calibration coefficient,  $\eta$ , which represents the relationship between the unit camera gray value and the number of received photons, was calibrated using a standard tungsten lamp. The corrected gray value  $I_m/f$  could then be used instead of the original gray value for the reconstruction. A quantitative chemiluminescence distribution was thus obtained without changing the 3D-CTC system.

A CH<sub>4</sub>/air flat flame experiment was performed to evaluate the proposed correction method. The reconstructed result with correction was highly uniform and was closer to the theoretical situation than the result without correction. This means that the proposed method can overcome the artificial distortion caused by uncorrected reconstruction. A cube phantom with uniform illumination was then used to simulate the effect of the correction. The results show that the reconstruction error without correction initially decreases and then increases along with the emission intensity of the voxel. The maximum error exceeds 50% in the low-response nonlinear region, while the reconstruction error with correction changed slightly for all emission intensities. These improvements may provide 3D-CTC with an accurate measurement ability for engine monitoring and for verification of numerical simulations of combustion.

**Funding.** National Natural Science Foundation of China (11372329, 11802315, 11927803); Youth Innovation Promotion Association of the Chinese Academy of Sciences (2018023).

**Acknowledgment.** We thank David MacDonald, MSc, from Liwen Bianji, Edanz Editing China (www.liwenbianji.cn/ac), for editing the English text of a draft of this paper.

**Disclosures.** The authors declare no conflicts of interest.

## REFERENCES

- J. Floyd, "Computed tomography of chemiluminescence: a 3D time resolved sensor for turbulent combustion," Ph.D. thesis (Imperial College, 2009).
- Q. Lei, Y. Wu, W. Xu, and L. Ma, "Development and validation of a reconstruction algorithm for three-dimensional nonlinear tomography problems," *Opt. Express* **24**, 15912–15926 (2016).
- J. Floyd and A. M. Kempf, "Computed tomography of chemiluminescence (CTC): high resolution and instantaneous 3-D measurements of a matrix burner," *Proc. Combust. Inst.* **33**, 751–758 (2011).
- J. Floyd, P. Geipel, and A. Kempf, "Computed tomography of chemiluminescence (CTC): instantaneous 3D measurements and phantom studies of a turbulent opposed jet flame," *Combust. Flame* **158**, 376–391 (2011).
- M. Kang, X. Li, and L. Ma, "Three-dimensional flame measurements using fiber-based endoscopes," *Proc. Combust. Inst.* **35**, 3821–3828 (2015).
- M. Kang, Y. Wu, and L. Ma, "Fiber-based endoscopes for 3D combustion measurements: view registration and spatial resolution," *Combust. Flame* **161**, 3063–3072 (2014).
- L. Ma, Q. Lei, Y. Wu, T. M. Ombrello, and C. D. Carter, "3D measurements of ignition processes at 20 kHz in a supersonic combustor," *Appl. Phys. B* **119**, 313–318 (2015).
- L. Ma, Y. Wu, Q. Lei, W. Xu, and C. D. Carter, "3D flame topography and curvature measurements at 5 kHz on a premixed turbulent Bunsen flame," *Combust. Flame* **166**, 66–75 (2016).
- S. Candel, "Combustion dynamics and control: progress and challenges," *Proc. Combust. Inst.* **29**, 1–28 (2002).
- K. T. Walsh, J. Fielding, M. D. Smooke, M. B. Long, and A. Liñán, "A comparison of computational and experimental lift-off heights of coflow laminar diffusion flames," *Proc. Combust. Inst.* **30**, 357–365 (2005).
- M. J. Bedard, T. L. Fuller, S. Sardeshmukh, and W. Anderson, "Chemiluminescence as a diagnostic in studying combustion instability in a practical combustor," *Combust. Flame* **213**, 211–225 (2020).
- J. S. Hardi, W. Z. Hallum, C. Huang, and W. E. Anderson, "Approaches for comparing numerical simulation of combustion instability and flame imaging," *J. Propul. Power* **32**, 279–294 (2016).
- T. Fiala and T. Sattelmayer, "On the use of OH\* radiation as a marker for the heat release rate in high-pressure hydrogen liquid rocket combustion," in *49th AIAA/ASME/SAE/ASEE Joint Propulsion Conference* (2013), p. 3780.
- S. V. Sardeshmukh, S. D. Heister, and W. E. Anderson, "Prediction of combustion instability with detailed chemical kinetics," in *53rd AIAA Aerospace Sciences Meeting* (2015), p. 1826.
- J. C. Dunlap, M. M. Blouke, E. Bodegom, and R. Widenhorn, "Modeling nonlinear dark current behavior in CCDs," *IEEE Trans. Electron Devices* **59**, 1114–1122 (2012).
- R. Widenhorn, J. C. Dunlap, and E. Bodegom, "Exposure time dependence of dark current in CCD imagers," *IEEE Trans. Electron Devices* **57**, 581–587 (2010).
- A. Piterman and Z. Ninkov, "Sub-pixel sensitivity maps for a back-illuminated CCD and the effects of non-uniform response on measurement accuracy," *Opt. Eng.* **41**, 1192–1202 (2002).
- D. Kavaldjiev and Z. Ninkov, "Influence of non-uniform CCD pixel response on aperture photometry," *Opt. Eng.* **40**, 162–169 (2001).
- N. S. Qiao, "Nonlinearity of CCD and its adjustment," *Acta Photonica Sin.* **11**, 2305–2309 (2008).
- W. Cai, X. Li, F. Li, and L. Ma, "Numerical and experimental validation of a three-dimensional combustion diagnostic based on tomographic chemiluminescence," *Opt. Express* **21**, 7050–7064 (2013).
- T. Yu, Z. Li, C. Ruan, F. Chen, X. Lu, and W. Cai, "Development of an absorption-corrected method for 3D computed tomography of chemiluminescence," *Meas. Sci. Technol.* **30**, 045403 (2019).
- E. R. Fossum and D. B. Hondongwa, "A review of the pinned photodiode for CCD and CMOS image sensors," *IEEE J. Electron Devices Soc.* **2**, 33–43 (2014).
- Y. Ishino and N. Ohiwa, "Three-dimensional computerized tomographic reconstruction of instantaneous distribution of chemiluminescence of a turbulent premixed flame," *JSME Int. J. B* **48**, 34–40 (2005).
- K. Wang, F. Li, P. Zou, X. Lin, R. Mao, and X. Yu, "Effect of the fuel-air flow velocity on heat release rate of swirling non-premixed methane flames," *Aerospace Sci. Technol.* **95**, 105465 (2019).
- K. Wang, F. Li, H. Zeng, and X. Yu, "Three-dimensional flame measurements with large field angle," *Opt. Express* **25**, 21008–21018 (2017).
- H. Faraji and W. J. MacLean, "CCD noise removal in digital images," *IEEE Trans. Image Process.* **15**, 2676–2685 (2006).
- Y. Tsin, V. Ramesh, and T. Kanade, "Statistical calibration of CCD imaging process," in *8th IEEE International Conference on Computer Vision (ICCV)* (IEEE, 2001), pp. 480–487.
- D. Montgomery, R. Drake, B. Jones, and J. Wiedwald, "Flat-field response and geometric distortion measurements of optical streak cameras," *Proc. SPIE* **0832**, 283–288 (1988).
- R. Turner, O. Landen, D. Bradley, S. Alvarez, P. Bell, R. Costa, J. Moody, and D. Lee, "Comparison of charge coupled device vs film readouts for gated micro-channel plate cameras," *Rev. Sci. Instrum.* **72**, 706–708 (2001).
- M. M. Hossain, G. Lu, and Y. Yan, "Three-dimensional reconstruction of combustion flames through optical fiber sensing and CCD imaging," in *Instrumentation and Measurement Technology Conference (I2MTC)* (IEEE, 2011).

31. Z. Xin, L. Jiaming, Z. Zhe, Q. Zhifeng, G. Yi, and S. Dingguo, "Research on image plane uniformity measurement technology of large field of view CCD imaging system," *Optics* **31**, 846–848 (2005).
32. G. Zhenhua, X. Baoping, D. Min, G. Yueming, and Y. Piyin, "Curve fitting of CCD opto-electronic response based on neural dynamics," *Opto-Electron. Eng.* **43**, 52–57 (2016).
33. W. Jia, G. Shenhui, and L. Li, "Uncertainty analysis of calibrating a reference standard," *Metrol. Technol.* **2018**, 60–61.
34. B. Wu and C. X. Fu, "Calibration experiment for intensity response characteristics of digital color camera," *Opto-Electro. Eng.* **33**, 101–105 (2006).
35. T. C. Williams and C. R. Shaddix, "Simultaneous correction of flat field and nonlinearity response of intensified charge-coupled devices," *Rev. Sci. Instrum.* **78**, 123702 (2007).
36. J.-W. Ren, Y.-Q. Zhang, Z. Ye, and X.-R. Quan, "Establishment and application of CCD radiation response function matrix," *Guangxue Jingmi Gongcheng (Opt. Precis. Eng.)* **20**, 957–962 (2012).
37. K. Wang, F. Li, Y. Wu, and X. Yu, "Quantitative measurements of chemiluminescence in a laminar methane–air premixed flame and comparison to numerical methods," *Energy Fuels* **32**, 5536–5543 (2018).
38. J. Wiedwald and R. Lerche, "Streak camera dynamic range optimization," *Proc. SPIE* **0832**, 275–282 (1988).
39. X. Li and L. Ma, "Volumetric imaging of turbulent reactive flows at kHz based on computed tomography," *Opt. Express* **22**, 4768–4778 (2014).
40. D. Y. W. F. C. Shou, "Nonlinear response measurement of planar CCD," *J. Ordnance Eng. Coll.* **4**, 35–42 (2001).
41. L. J. Xue, T. Z. Li, C. L. Li, Y. Z. Ji, Y. Cui, and Z. H. Wang, "Study on the hyper-spectral CCD imager non-uniformity correction algorithm," *Acta Photonica Sin.* **35**, 693–696 (2006).
42. Y.-J. Chen, Z.-J. Zhang, and Z.-Q. Zhang, "Correction of CCD pixel nonuniformity," *Opt. Precis. Eng.* **2**, 216–220 (2004).
43. M. Mekhregin, V. Guryev, I. Meshkovskii, D. Smirnov, and A. Sukhinets, "Development of sensor for spectral monitoring of combustion processes in gas-turbine engines," in *IEEE East-West Design & Test Symposium (EWDTS)* (IEEE, 2018), pp. 1–4.
44. C. Ruan, F. Chen, W. Cai, Y. Qian, L. Yu, and X. Lu, "Principles of non-intrusive diagnostic techniques and their applications for fundamental studies of combustion instabilities in gas turbine combustors: a brief review," *Aerospace Sci. Technol.* **84**, 585–603 (2019).
45. C. Shi, C. Ji, S. Wang, J. Yang, X. Li, and Y. Ge, "Numerical simulation on combustion process of a hydrogen direct- injection stratified gasoline Wankel engine by synchronous and asynchronous ignition modes," *Energy Convers. Manage.* **183**, 14–25 (2019).